DOI: 10.15480/882.9348

Eighth International Symposium on Marine Propulsors
smp'24, Berlin, Germany, March 2024

Unsteady evolution of a trailing vortex subject to time-varying inflow boundary conditions

Mark A. Herndon[1], **Justin W. Jaworski**[2]

[1]Department of Mechanical Engineering and Mechanics, Lehigh University, Bethlehem, PA 18015, USA
[2]Department of Aerospace and Ocean Engineering, Virginia Polytechnic Institute and State University, Blacksburg, VA 24061, USA

ABSTRACT

A Batchelor vortex is prescribed as an inflow boundary condition for high-fidelity fluid dynamics simulations to investigate the influence of upstream vortex motions on the vortex evolution downstream. This configuration emulates the unsteady motions of a lifting surface that induce small perturbations to the initial state of a trailing vortex and can evolve into large three-dimensional deformations downstream. The computational campaign characterizes the downstream evolution of a canonical trailing vortex model subject to low-amplitude periodic oscillations of the center position over a range of Strouhal numbers. Periodic oscillations of the vortex center position in one or two simultaneous directions introduce curvature to the trailing vortex system, whose self-induced rotation creates non-planar sinusoidal deformations of the vortex in the streamwise direction at long times that deviate from the well-known planar rotation of linear theory. Phase snapshots of this canonical streamwise vortex configuration prescribed harmonically at the inflow boundary are expected to elucidate the unsteady character of a real trailing vortex generated by a propellor or control surface in the absence of wake effects. Growth of the vortex perturbation amplitude is not observed in the present computations, in contrast to available experimental data, which suggests that pure translational motions of a single vortex are not sufficient to excite perturbation amplitude growth.

Vortex dynamics

1 INTRODUCTION

The unsteady evolution of trailing vortices is highly relevant to hydrodynamic and aerodynamic engineering applications. The interactions of an unsteady trailing vortex with downstream bodies can produce significant unsteady loading and are generally undesirable, which motivate an improved understanding of vortex evolution that is critical for load anticipation and control (Garmann and Visbal, 2015). In pursuit of this goal, Fishman and Rockwell (2018) investigated the onset and development of orbital motion of a trailing vortex subject to small-amplitude heaving motions over a range of Strouhal numbers. The small-amplitude heaving motion of the airfoil perturbs the location and flow characteristics of the trailing vortex, which may undergo significant changes as the vortex evolves downstream. At low Strouhal number, the motion of the vortex remains nearly uni-directional with small variations in axial velocity along the vortex core. The geometric excursion of the vortex also shows no amplification as it advects downstream, which is in stark contrast to the vortex behavior at high Strouhal numbers. At high Strouhal number, Fishman et al. (2017) found the trailing vortex excursion amplitude increases by up to a factor of 10 in the streamwise direction, with pronounced variations in axial velocity along the core and increased curvature in the vortex topology. The increase in vortex curvature is strongly associated with changes in axial velocity deficit and vorticity, as changes in these parameters affect the swirl ratio, q. The swirl ratio q measures the ratio between vortex strength and axial velocity deficit, and is mathematically defined as $q = \Gamma_0/(2\pi r_0 \Delta u)$ where Γ_0 is the vortex strength, r_0 is the vortex core radius, and Δu is the axial velocity deficit. Leibovich and Stewartson (1983) demonstrated that a Batchelor vortex is unstable when $q \leq \sqrt{2}$, which for a vortex with fluctuating circulation strengths and axial velocity deficit can create locally unstable regions along the length of the vortex.

A complementary computational effort was performed by Garmann and Visbal (2017), where low-amplitude, high-frequency oscillations of a NACA0012 wing were shown to alter the initial state of the trailing vortex as it leaves the wing. The vortex is laterally displaced throughout the oscillation cycle of the wing, leading to the pronounced bi-directional motion of the vortex, where the vortex also undergoes significant fluctuations in axial velocity deficit and axial vorticity magnitude. The amplification of vortex deformations downstream corresponded to enhanced orbital motion of the trailing vortex, which can be characterized by non-planar sinusoidal deformations of the mean vortex centerline.

The present research seeks to further characterize the far-field evolution of a perturbed trailing vortex subject to time-varying initial conditions. Specifically, the present computational work seeks to clarify which features of the vortex evolution are due to its translational movement at the point of generation, or may be the result of time-dependent changes in the vortex state or flow details extended to the vortex when generated. The topological changes to the vortex trajectory are explored, where the vortex is subject to small periodic translations of the vortex center position only. Variations in vortex strength and axial velocity deficit are not considered in the present paper to focus solely on the role of vortex translation and its effects on trajectory amplification.

2 NUMERICAL PROCEDURE

The governing equations of fluid motion to be solved are the three-dimensional, compressible Navier-Stokes equations. These equations are cast into strong conservation form after a general time-dependent coordinate transformation from Cartesian space (x, y, z, t) to computational space (ξ, η, ζ, τ) and are written as

$$\begin{aligned} \frac{\partial \hat{\mathbf{Q}}}{\partial \tau} + \frac{\partial}{\partial \xi}\left(\hat{\mathbf{F}} - \frac{1}{Re}\hat{\mathbf{F}}_v\right) + \frac{\partial}{\partial \eta}\left(\hat{\mathbf{G}} - \frac{1}{Re}\hat{\mathbf{G}}_v\right) \\ + \frac{\partial}{\partial \zeta}\left(\hat{\mathbf{H}} - \frac{1}{Re}\hat{\mathbf{H}}_v\right) = 0, \end{aligned} \tag{1}$$

where the vector of dependent variables is

$$\hat{\mathbf{Q}} = \frac{1}{J}\left[\rho, \rho u, \rho v, \rho w, \rho e\right]^T, \tag{2}$$

and *Re* is the characteristic Reynolds number. The governing equations are written in terms of non-dimensional variables, where ρ is the density, u, v, and w are the Cartesian components of the velocity, and e is the specific internal energy. All variables are normalized with respect to their reference values except for pressure, which is normalized by twice the freestream dynamic pressure $\rho_\infty U_\infty^2$. Definitions for the inviscid and viscous fluxes, $\hat{\mathbf{F}}$, $\hat{\mathbf{G}}$, $\hat{\mathbf{H}}$ and $\hat{\mathbf{F}}_v$, $\hat{\mathbf{G}}_v$, $\hat{\mathbf{H}}_v$ are not shown here for brevity, but can be found in Tannehill et al. (1997), for example.

Solutions to Equation 1 are obtained by the implicit approximately factored finite-difference algorithm of Beam and Warming (1978), where efficiency in the solution procedure is gained via the improved diagonalization of Pulliam et al. (2020). Numerical errors due to the factorization and diagonalization procedure are then eliminated by the use of Newton-like subiterations.

Spatial derivatives are computed by sixth-order compact finite-differences, and an eighth-order low-pass filter is applied to the solution variables at each time step to eliminate high-frequency solution components of which may be poorly resolved due to the mesh size (Visbal and Gaitonde, 1999; Visbal and Rizzetta, 2002). This implicit large-eddy-simulation (ILES) methodology provides a uniform computational approach across flow regimes where the equations and methodology are unchanged for laminar, transitional, and turbulent flows. Further details on the present ILES methodology can be found in Visbal et al. (2003) and Rizzetta and Visbal (2018).

The solution procedure is carried out using the AFRL FDL3DI computational fluid dynamics solver, which employs the described high-fidelity ILES technique. The ILES procedure is leveraged to provide robust numerical realization of unsteady flow features that would be otherwise difficult to measure in an experiment.

3 PROBLEM CONFIGURATION

A simplified vortex model is cast as an inflow boundary condition to study how small geometric perturbations to the vortex center position influence downstream evolution. Figure 1 shows the generic problem setup, where a vortex advects into the computational domain and is permitted to evolve in space and time. The selected vortex model is the Batchelor q-vortex, where the azimuthal velocity profile is given as

$$u_\theta = \frac{q\,\Delta u}{r/r_0}\left(1 - \exp\left(-(r/r_0)^2\right)\right), \tag{3}$$

with axial velocity

$$u_z = 1 - \Delta u \exp\left(-(r/r_0)^2\right), \tag{4}$$

where q is proportional to the ratio between vortex strength Γ and the axial velocity deficit, Δu (Batchelor, 1964). The unsteady radial position r is implicitly defined as

$$r = r(t) = \sqrt{(x - x_c(t))^2 + (y - y_c(t))^2}, \tag{5}$$

where x_c and y_c are the time-dependent vortex center positions, and r_0 is the vortex core radius. The vortex parameters q, Δu, and r_0 may also be treated as time-dependent, but are considered constant in the present study.

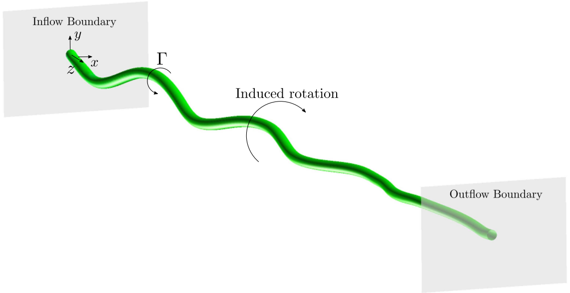

Figure 1: Representative streamwise vortex with time-varying inflow center-position. Imposed lateral displacements at the inflow boundary lead to self-induced rotation of the vortex downstream.

The parameters for the vortex core size in the base profile are in accordance with Fishman et al. (2017) and Fishman and Rockwell (2018) at $d_0 = 0.1$, where d_0 is twice the vortex core radius r_0. The vortex core diameter d_0 is selected as the characteristic length scale, where the coordinates $\hat{x}$, $\hat{y}$, and $\hat{z}$ are the x, y, and z coordinates scaled respectively by d_0. The Reynolds number is in alignment with Fishman and Rockwell (2018), where their chord based Reynolds number $Re_c = 15200$ corresponds to Reynolds number $Re_{d_0} = 1520$ based on the vortex diameter. A low freestream Mach number has been selected as $M_\infty = 0.1$ to minimize the effects of compressibility, which are not examined in this study.

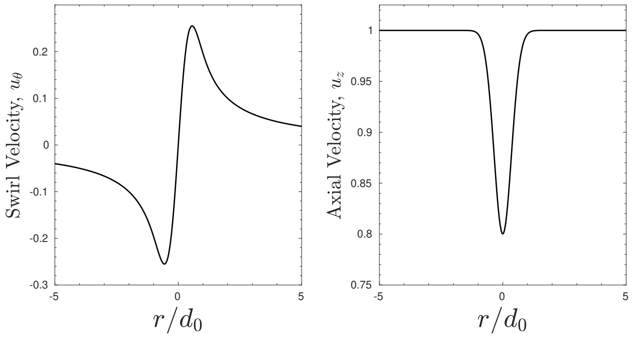

Figure 2: Velocity profiles of the vortex at the inflow boundary to be used in all computations, where only the center position is varied.

Figure 2 illustrates the swirl and axial flow profiles, which are used without change throughout the oscillation cycle for all frequencies considered. The Strouhal number is defined by $St = fd_0/U_\infty$, where f is the frequency of oscillation and U_∞ is the freestream velocity. The present set of Strouhal numbers are within the range of experiments carried out by Fishman and Rockwell (2018), where their Strouhal number was defined with the length scale specified as the chord length c ($St_{d_0} = 0.1 St_c$).

The vortex center coordinates at the inflow boundary oscillate in phase according to

$$x_{c_0}(t) = A_x \sin(2\pi St_x \tau) \quad (6)$$

$$y_{c_0}(t) = -A_y \cos(2\pi St_y \tau), \quad (7)$$

which positions the vortex at $\hat{x} = 0$ and $\hat{y} = -A_y/d_0$ at $\tau = 0$.

Table 1: Parameters for uni- and bi-directional vortex motion with constant flow profile.

A_x/d_0	A_y/d_0	St_x	St_y	q	Δu	d_0
-	0.3	-	0.01	2	0.2	0.1
-	0.3	-	0.025	2	0.2	0.1
-	0.3	-	0.05	2	0.2	0.1
-	0.3	-	0.07	2	0.2	0.1
0.4	0.3	0.01	0.01	2	0.2	0.1
0.4	0.3	0.025	0.025	2	0.2	0.1
0.4	0.3	0.05	0.05	2	0.2	0.1
0.4	0.3	0.07	0.07	2	0.2	0.1

The non-dimensional x and y amplitudes, Strouhal numbers, and vortex flow profiles are provided in Table 1.

4 DETAILS OF THE COMPUTATIONS

Three computational grids were constructed to study the effect of spatial resolution and establish confidence in a numerically converged solution. The highest frequency case of uni-directional motion is considered for the grid resolution study, as this will also be the limiting case for the selected time step of $\Delta\tau = \mathbf{0.005}$ where $\tau = tU_\infty/d_0$. This selection leads to 2,856 time steps per oscillation cycle for the highest frequency case. The low value of $\Delta\tau$ yields a Courant-Friedrichs-Lewy (CFL) number of $N_{\text{CFL}} = 0.0757$ based on the medium streamwise grid spacing and an inflow velocity of unity, and a CFL number of $N_{\text{CFL}} = 0.041$ based on the maximum swirl velocity and medium grid spacing across the vortex flow profile. The low values of CFL number provide confidence that the simulations are stable with respect to the time step and are adequately resolved for the evolution of laminar vortices (Demuren and Ibraheem, 1994).

Table 2: Details of the computational grids. $\Delta\hat{x}_{\text{core}} = \Delta\hat{y}_{\text{core}}$ is the constant spacing across the vortex core region normalized by the vortex core diameter, and $\Delta\hat{z}$ is the normalized spacing in the streamwise direction. The constant spacing in the vortex core region extents $\pm 5d_0$ from the (x, y) origin on each streamwise plane, where the spacing is then slowly stretched out to the far-field boundaries 800d_0 away. The total points for the coarse, medium, and fine grids are 11,844,150 points, 51,418,800 points, and 135,136,800 points, respectively.

Mesh	n_ξ	n_η	n_ζ	$\Delta\hat{x}_{\text{core}}$	$\Delta\hat{z}$
Coarse	281	281	150	6e-2	0.133
Medium	414	414	300	3e-2	0.066
Fine	548	548	450	2e-2	0.044

Table 2 shows the level of refinement and spatial resolution for the coarse, medium, and fine grids, respectively. The medium grid is uniformly twice as refined as the coarse grid, and the fine grid is 1.5 times as refined as the medium. The grid is constructed in Cartesian coordinates with a refined region in the vicinity of the vortex, which is then stretched out to the far-field boundaries to minimize excessive grid points.

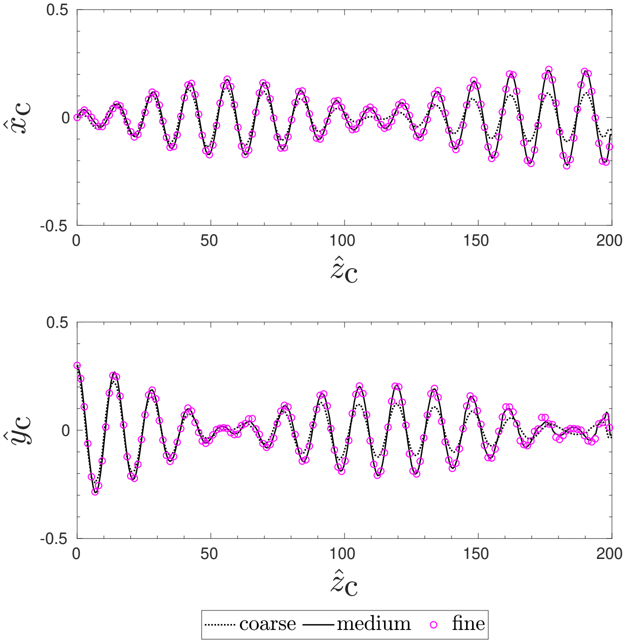

Figure 3: Center positions for the highest frequency St= 0.07 uni-directional motion case were considered for the grid convergence study. Convergence is demonstrated for the normalized $\hat{x}$ and $\hat{y}$ coordinates along the streamwise direction at a select instant in time, $\tau = 300$.

The primary quantity of interest is the location of the vortex center position as a function of streamwise position, hence examining its convergence with the varying grids is paramount. The vortex center position is selected as the local pressure minimum on each streamwise plane. Figures 3 and 4 show the center position as a function of streamwise distance at a select instant in time and as a periodic function on select streamwise planes.

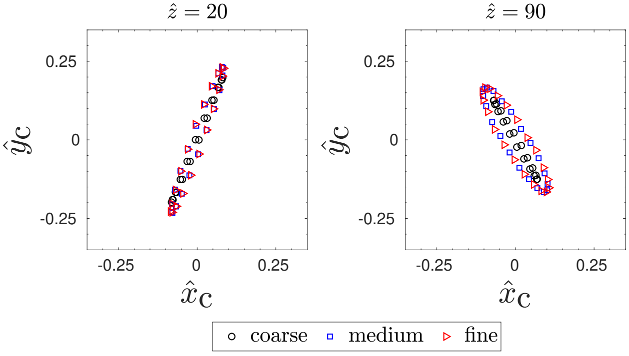

Figure 4: The periodic traces of the vortex center positions are shown to be converged for the uni-directional case St= 0.07 at two streamwise planes. The coarse grid under predicts the magnitude of orbital motion at increasing streamwise distance.

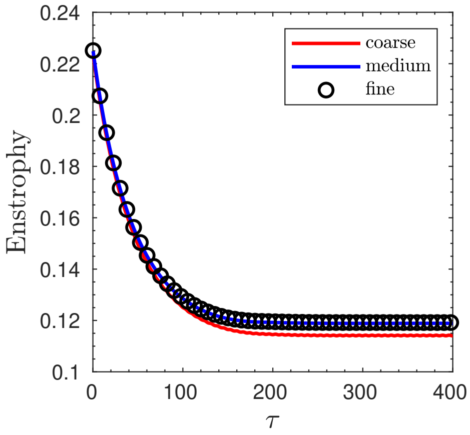

Figure 5: Integrated quantity of enstrophy over the entire computational domain with respect to time shows the system ramp down to steady-state for all grids considered, where convergence is demonstrated for the medium grid.

The integrated quantity of enstrophy is also measured to ensure global convergence of the flow field, where Fig. 5 demonstrates convergence for the medium grid. The enstrophy, $\mathcal{E}$, is computed numerically from the vorticity field $\boldsymbol{\omega}$ over the entire computational volume $\mathcal{V}$ according to

$$\mathcal{E} = \int_{\mathcal{V}} (\boldsymbol{\omega} \cdot \boldsymbol{\omega}) \, \mathrm{d}\mathcal{V}. \tag{8}$$

From $\tau = 0$ to $\tau = 200$, the flow field adjusts to a periodic state as the inflow perturbations propagate to the outflow boundary. After the initial flow profile reaches the outflow boundary, the energy entering and leaving the system remains constant, which yields the ramp down to a constant value for the enstrophy. Quantities such as the turbulent kinetic energy may also be considered; however, this study considers laminar vortex profiles with no added noise. The enstrophy of the system is proportional to the decay in kinetic energy of the system, which achieves equilibrium after the initial transient. The medium grid is confidently selected for the remainder of the studies herein.

5 RESULTS

This section presents results for a series of simulations detailed in Table 1. The parameters for the present set of simulations are inspired by Fishman and Rockwell (2018), where a NACA0012 wing heaves at varying frequencies with a constant amplitude of 3% the airfoil chord length. The 3% chord length parameter is the basis for the uni-directional motion amplitude in the y-direction, which corresponds to amplitudes of 0.3 times the vortex core diameter. Fishman and Rockwell (2018) also observed lateral excursions of 4% of the airfoil chord during the oscillation cycle for their highest frequency case, which corresponds to 0.4 times the vortex core diameter. Results are delineated by its phase, Φ, in the unsteady cycle of the imposed vortex motion. The phases are relative to the time origin $\tau = 200$, where each phase increment corresponds to one eighth of an oscillation period advancement in time.

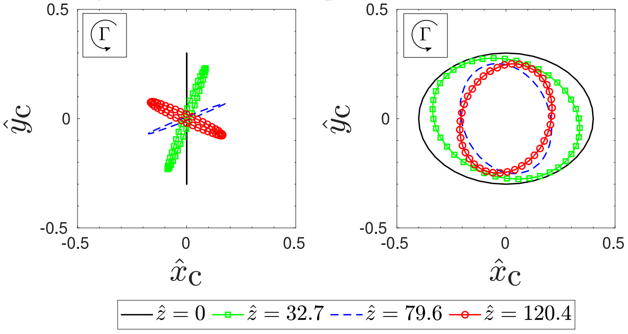

Figure 6: Traces of vortex center position at various downstream locations for both uni-directional (left) and bi-directional (right) motion at St= 0.05. The vortex traverses the elliptical paths in the counter-clockwise direction on each downstream plane, where the axis of the elliptical paths rotate clockwise with increasing streamwise distance.

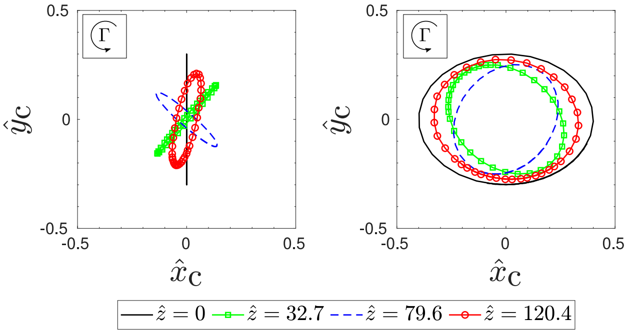

Figure 7: Traces of vortex center position at various downstream locations for both uni-directional (left) and bi-directional (right) motion at St= 0.07.

The characteristic paths for each Strouhal number considered are qualitatively similar, where periodic traces of the vortex center position are only shown for the two highest Strouhal number cases for illustrative purposes. Figures 6 and 7 show the periodic traces of the vortex center position at various downstream locations for the two highest Strouhal number cases. For uni-directional motion, the elliptical trace of the vortex rotates in the clockwise direction at each successive streamwise plane, which can be attributed to the self-induced rotation of a curved vortex (Hama, 1963; Bliss, 1970). The minor axis of the elliptical paths traced out by the vortex increases with downstream distance, and is more prominent at higher frequencies. The induced lateral motion of the vortex is a function of streamwise distance, where the cases of higher frequency achieve greater rotation sooner. For bi-directional motion, the vortex traces out elliptical paths in the counterclockwise direction on a constant downstream plane, where the major axis of the ellipses rotates in the clockwise direction with downstream distance. The path tracing direction of the vortex and the rotation of the elliptical axis with streamwise distance is consistent across uni- and bi-directional cases.

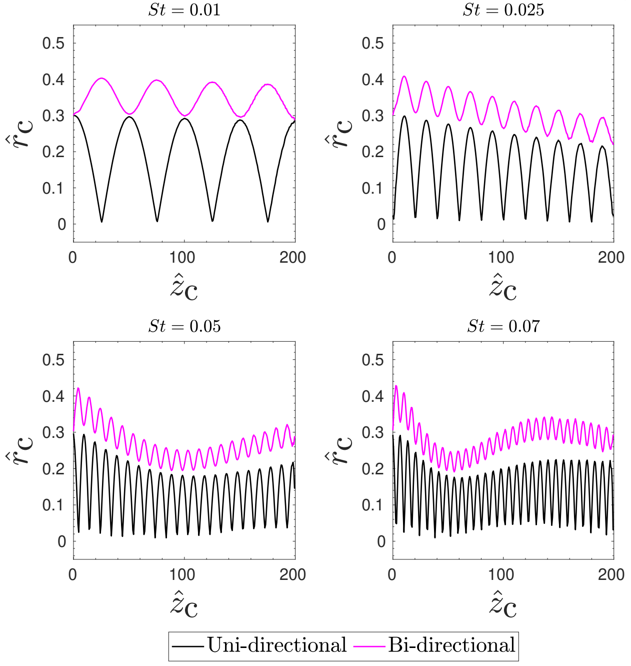

Figure 8: Local radial distance away from the origin, denoted by $\hat{r}_c$, per streamwise plane for uni- and bi-directional motion at Strouhal numbers 0.05 and 0.07.

The prescribed oscillations at the inflow boundary are centered at the origin, hence radial displacements from the center of oscillation of the vortex center position are easily attainable at each streamwise plane. Figure 8 shows the local radius of the vortex center position as a function of streamwise distance at an arbitrary moment in time. The experimental results of Fishman and Rockwell (2018) indicate that amplification may occur for the higher Strouhal number case; however, amplification is not observed in the current study. For all cases, the peak radial displacement from the origin either remains constant or decreases with streamwise distance. As the Strouhal number increases, the radial displacement tends to decay with streamwise distance. For bi-directional motion, we observe a decrease in displacement amplitude and then a subsequent increase back towards the imposed displacement values. The vortices do not experience displacements greater than the prescribed motion at the inflow, which is in contrast to existing experimental work. The absence of amplification may be due to the constant flow profile of the vortex imposed in the current study, where experiments show large fluctuations in axial velocity deficit and circulation strength throughout the oscillation cycle.

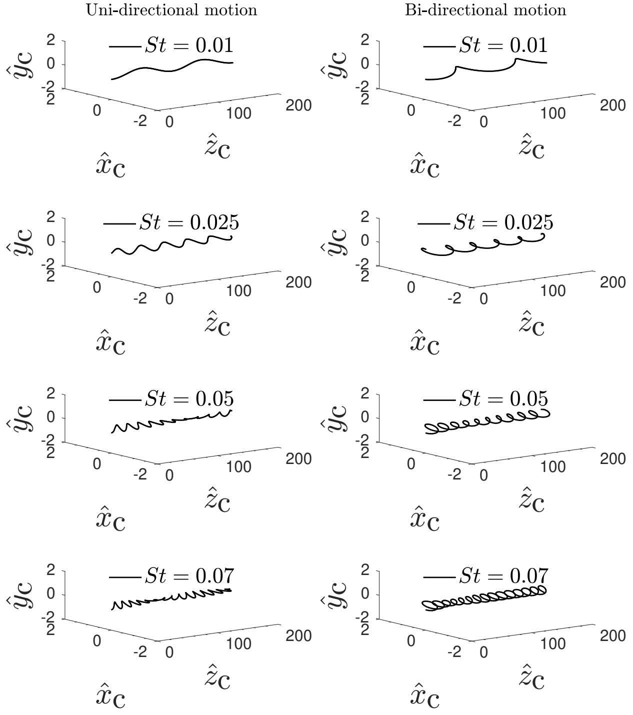

Figure 9: Line graphs of vortex center position

A three-dimensional representation of the vortex center positions at an arbitrary moment in time after reaching steady-state motions is shown in Fig. 9. The line graphs of the vortex center positions show that the center location method produces a stable vortex center and illuminates the basic topology of the vortex. As the Strouhal number increases, the self-induced rotation of the vortex becomes more evident for the uni-directional cases. The vortices rotate in the sense opposite of the vortex circulation, resulting in a non-planar deformation of the vortex centerline. Figures 10 and 13 provide three-dimensional representations of the vortex structure in terms of isosurfaces of Q-criterion at different phases of the oscillation cycle. The Q-criterion formulation of Hunt et al. (1988) is used in this work, where positive values of Q indicate a flow region where flow rotation is greater than the rate of strain. For a constant value of Q-criterion, $Q = 0.05$, the isosurface tapers with downstream distance as the vortex loses strength due to viscous dissipation. The axial velocity contours on the isosurfaces indicate fluctuations in magnitude along the length of the vortex. The axial velocity is not constant for a given value of Q-criterion, where the lower values of axial velocity are biased towards the outer edge of the elliptical path the vortex traces. This behavior is consistent across contours for both uni- and bi-directional cases, where the effects are most significant for the bi-directional case at $St = 0.07$. The greater variations in axial flow at the higher frequencies is in qualitative agreement with the experiments of Fishman et al. (2017), where higher frequency motions induce fluctuations in axial velocity throughout the oscillation cycle.

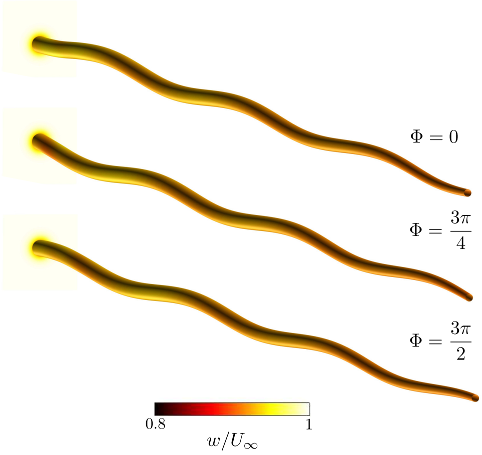

Figure 10: Isosurfaces of Q-criterion (Q= 0.05) for uni-directional vortex motion at St= 0.025 colored by axial velocity.

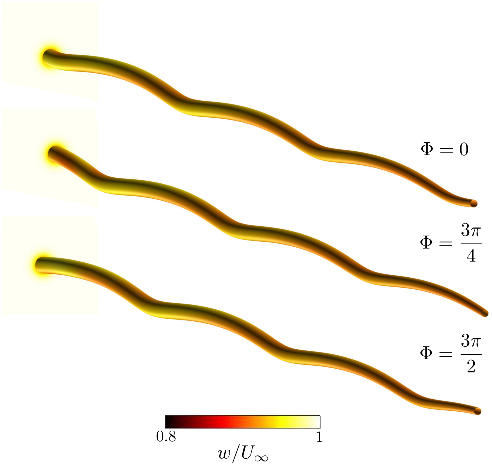

Figure 11: Isosurfaces of Q-criterion (Q= 0.05) for bi-directional vortex motion at a Strouhal number St= 0.025 colored by axial velocity.

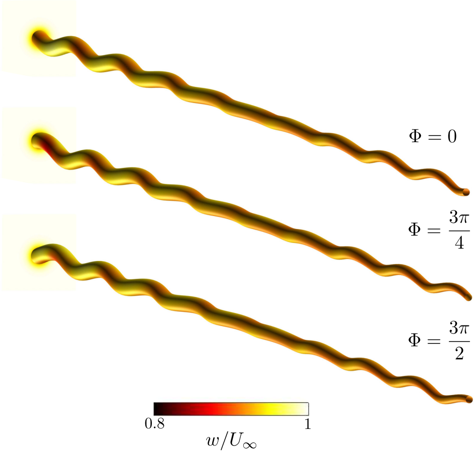

Figure 12: Isosurfaces of Q-criterion (Q= 0.05) for uni-directional vortex motion at St= 0.07 colored by axial velocity.

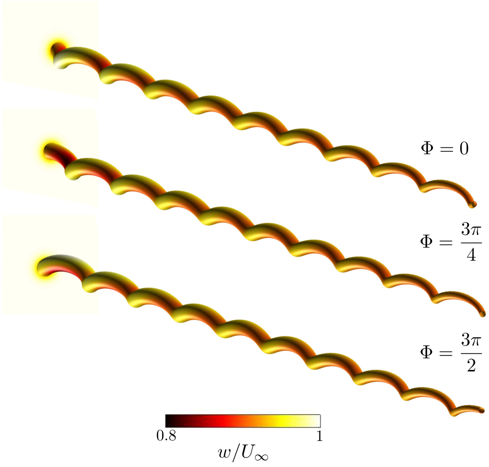

Figure 13: Isosurfaces of Q-criterion (Q= 0.05) for bi-directional vortex motion at St= 0.07 colored by axial velocity.

Figures 14-17 provide further detail on the axial flow across the vortex core at various streamwise locations, where the axial velocity (scaled by the freestream Mach number, $M_\infty = 0.1$) is plotted along the x-axis. The y-plane for each downstream location corresponds to the y-coordinate of the local pressure minimum at the given downstream location, providing the flow profile across the vortex core. For all cases, as the vortex evolves downstream, the magnitude of the axial velocity deficit decreases and the characteristic width of the flow profile increases, which is the expected behavior for steady Batchelor vortices (Batchelor, 1964). As the vortex moves downstream and undergoes its respective oscillation cycle, regions of accelerated flow beyond the freestream value outside of the vortex core are found. This effect becomes more pronounced with the higher Strouhal number cases, where the change in curvature of the vortex is much greater when compared to the lower Strouhal number cases. Uni-directional motion of the vortex at $St = 0.01$, for example, shows effectively no deviation of axial flow throughout the oscillation cycle. For bi-directional flow in Fig. 14, the magnitude of the axial velocity deficit remains relatively constant but is shifted laterally due to the imposed motion.

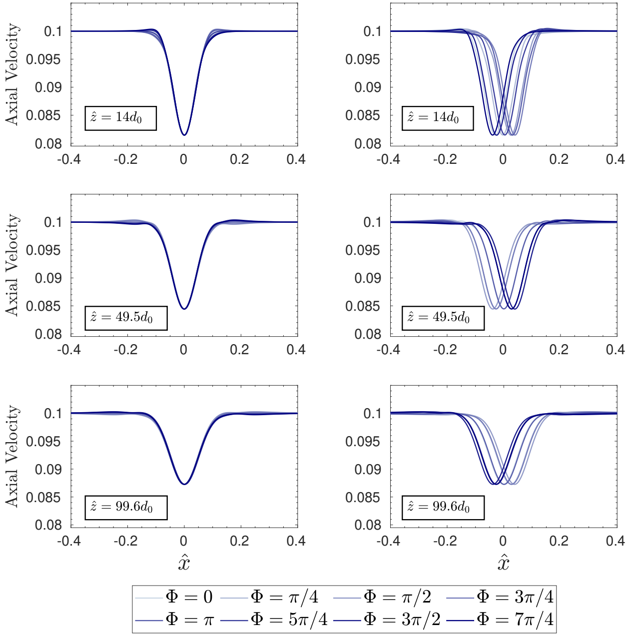

Figure 14: Axial velocity for uni- and bi-directional motion St= 0.01

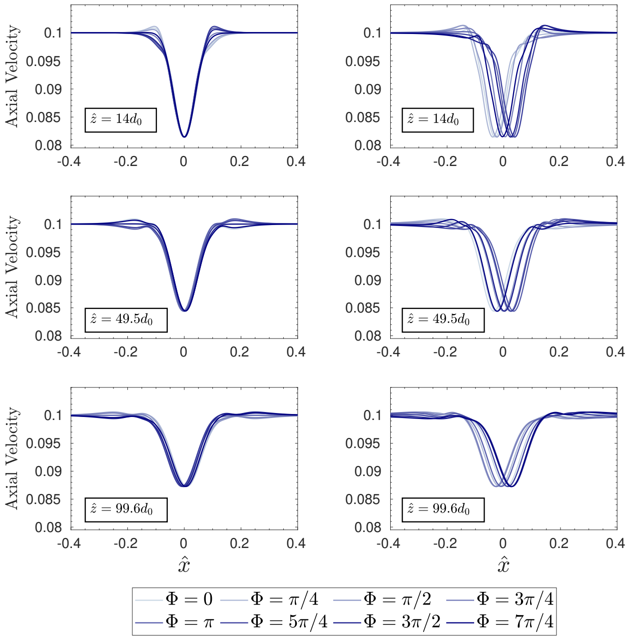

Figure 15: Axial velocity for uni- and bi-directional motion St= 0.025

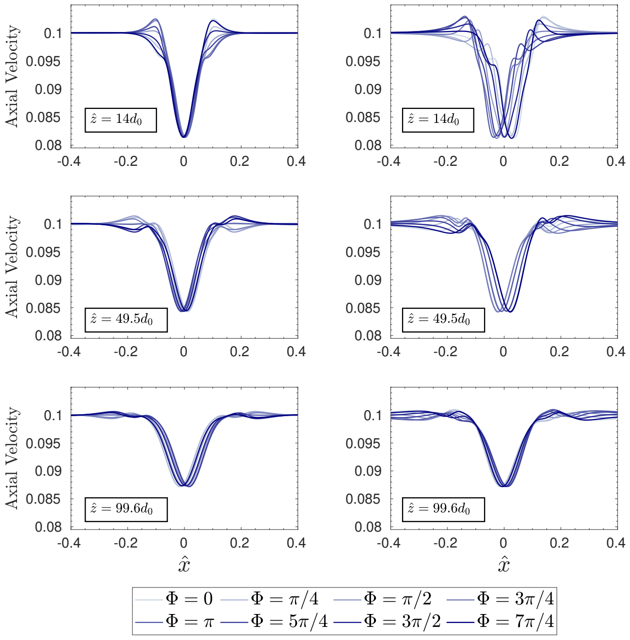

Figure 16: Axial velocity for uni- and bi-directional motion St= 0.05

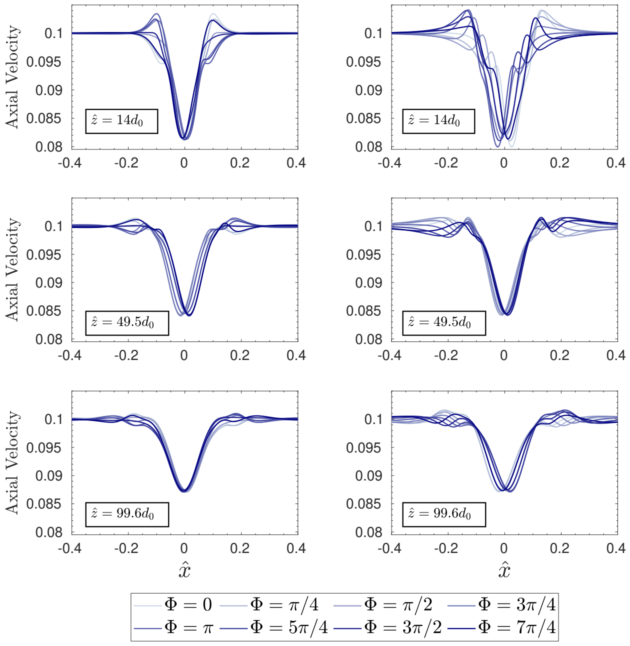

Figure 17: Axial velocity for uni- and bi-directional motion St= 0.07

Contours of axial velocity are shown in Figs. 18 and 19 for the highest Strouhal number case $St = 0.07$ for uni-directional motion and bi-direction motion respectively. The contours are taken 25 core diameters downstream from the inflow plane and are sequenced at equal phases in their oscillation cycles. Similar to the isosurfaces in Figs. 10-13, the axial velocity deficit is more pronounced towards the outer edge of the elliptical path.

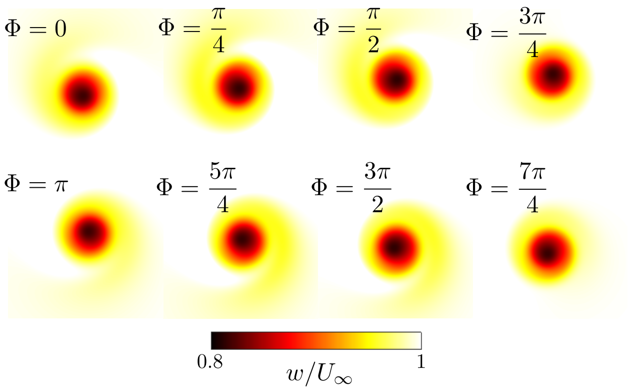

Figure 18: Contours of axial velocity during different phases of the oscillation cycle for uni-directional motion at $St = 0.07$.

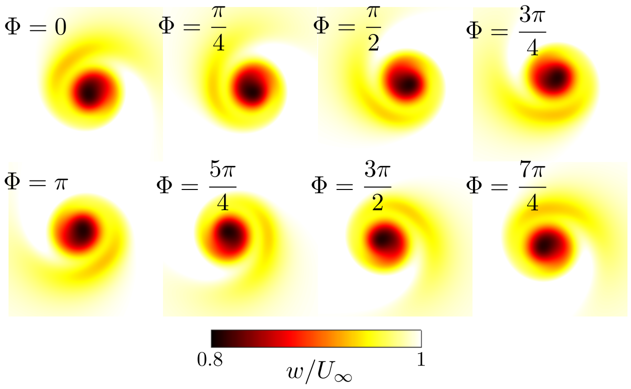

Figure 19: Contours of axial velocity during different phases of the oscillation cycle for bi-directional motion at $St = 0.07$.

6 CONCLUSIONS

A parametric sweep of oscillation frequency is carried out for prescribed uni- and bi-directional motions of a streamwise vortex, whose constant velocity profile is imposed as a translating inflow boundary condition in an otherwise uniform flow. The Strouhal numbers considered range from $St = 0.01$ to $St = 0.07$, which are the approximate low and high values explored in experimental and computational works of Fishman and Rockwell (2018) and Garmann and Visbal (2017), respectively.

Consistent across all cases is the self-induced rotation of the vortex trace in the clockwise direction as the vortex moves downstream, which is opposite to the circulation of the vortex. In a given downstream plane, the vortex traverses its periodic path in the counterclockwise direction. At low Strouhal number for uni-directional motion, the imposed vertical motion induces clockwise rotation as the vortex moves downstream; however, the plane of oscillation only rotates a few degrees by the time the vortex reaches the outflow due to the long wavelength of the motion. As Strouhal number increases, uni-directional motion promotes lateral displacements that are more apparent with increasing streamwise distance. Pronounced vortex curvature at higher Strouhal numbers corresponds to greater variations in the flow field and the vortex center traces.

For the current set of parameters of constant flow profile vortices subject only to small translations, self-induced amplification of the vortex trajectory is not observed. Pure translations of the vortex with a fixed flow profile lead to non-constant flow profiles as the vortex evolves downstream, but this adjustment by the flow field is not sufficient to replicate the growth observed for experimental trailing vortices generated by moving bodies.

ACKNOWLEDGMENTS

This work was supported by Office of Naval Research grant number N00014-23-1-2700, monitored by Dr. Yin Lu (Julie) Young. The authors also gratefully acknowledge the high-performance computer time and resources provided by the DoD High Performance Computing Modernization Program.

REFERENCES

Batchelor, G. K. Axial flow in trailing line vortices. *Journal of Fluid Mechanics*, 20(4):645–658, 1964.

Beam, R. M. and Warming, R. F. An implicit factored scheme for the compressible Navier-Stokes equations. *AIAA Journal*, 16(4):393–402, 1978.

Bliss, D. *The dynamics of curved rotational vortex lines.* PhD thesis, Massachusetts Institute of Technology, 1970.

Demuren, A. O. and Ibraheem, S. O. Stability analysis of factorization methods. *Numerical Heat Transfer, Part B Fundamentals*, 25(1):97–117, 1994.

Fishman, G. and Rockwell, D. Onset of orbital motion in a trailing vortex from an oscillating wing. *Journal of Fluid Mechanics*, 856:257–287, 2018.

Fishman, G., Wolfinger, M., and Rockwell, D. The structure of a trailing vortex from a perturbed wing. *Journal of Fluid Mechanics*, 824:701–721, 2017.

Garmann, D. J. and Visbal, M. R. Interactions of a streamwise-oriented vortex with a finite wing. *Journal of Fluid Mechanics*, 767:782–810, 2015.

Garmann, D. J. and Visbal, M. R. Analysis of tip vortex near-wake evolution for stationary and oscillating wings. *AIAA Journal*, 55(8):2686–2702, 2017.

Hama, F. R. Progressive deformation of a perturbed line vortex filament. *Physics of Fluids*, 6(4):526–534, 1963.

Hunt, J. C. R., Wray, A., and Moin, P. Eddies, streams, and convergence zones in turbulent flows. *Center for Turbulence Research Report*, 1988.

Leibovich, S. and Stewartson, K. A sufficient condition for the instability of columnar vortices. *Journal of Fluid Mechanics*, 126:335–356, 1983.

Pulliam, T. H., Jespersen, D. C., Bodony, D. J., and Bidadi, S. Improved eigenvectors for Pulliam-Chaussee diagonalized approximate-factorization algorithm. *Journal of Computational Physics*, 412:109443, 2020.

Rizzetta, D. P. and Visbal, M. R. An overset-mesh approach for large-eddy simulation of high-Reynolds number aerofoil flow. *International Journal of Computational Fluid Dynamics*, 32(6-7):293–314, 2018.

Tannehill, J. C., Anderson, D. A., and Pletcher, R. H. *Computational fluid mechanics and heat transfer*. Taylor & Francis, 1997.

Visbal, M. R. and Gaitonde, D. High-order-accurate methods for complex unsteady subsonic flows. *AIAA J.*, 37 (10):1231–1239, 1999.

Visbal, M. R. and Rizzetta, D. P. Large-eddy simulation on curvilinear grids using compact differencing and filtering schemes. *Journal of Fluids Engineering*, 124(4): 836–847, 2002.

Visbal, M. R., Morgan, P., and Rizzetta, D. P. An implicit LES approach based on high-order compact differencing and filtering schemes. In *16*$^{\text{th}}$ *AIAA Computational Fluid Dynamics Conference*. AIAA Paper 2003-4098, 2003.